Nonlinear Dyn
https://doi.org/10.1007/s11071-024-09726-1

RESEARCH

Application of nonlinear energy sink in suppressing wheel shimmy for advanced vehicle chassis design under independent wheel subsystems

Hangyu Lu · Giuseppe Habib · Xiaodong Wu · Yuankai Ren · Liang Yan

Received: 18 February 2024 / Accepted: 6 May 2024

Abstract Novel structures in vehicle control-by-wire chassis have re-emphasized the problem of wheel shimmy. Proper suppression of shimmy in the independent wheel subsystems would significantly improve the performance of the steer-by-wire control. In this paper, a wheel shimmy suppression method using a nonlinear energy sink (NES) is proposed. Compared with traditional methods of increasing steering damping, the NES seldom interferes with the designed steering dynamics of the vehicle due to its particularly small mass and volume, thus reserving availability for in-service or after-designed vehicles. By installing the NES in the wheel frame, a single towed wheel model with NES is constructed. Although the NES has almost no effect on the linear stability characteristics, an excellent effect on suppressing vibration amplitudes is explored where over 90% oscillation amplitude of shimmy is mitigated by the NES within a wide range of reasonable parameters. Parameter optimization for the NES global dynamics is performed to handle the speed-dependent nature of shimmy, and the result highlights its effectiveness and parameter robustness. Integration of the single-wheel model into the full vehicle with independent steering structures summarizes that the NES could be a favorable way to both suppress the existing shimmy phenomenon and control the coupled lateral oscillations of the vehicle body.

Keywords Wheel shimmy · Self-excited vibrations · Nonlinear energy sink · Vibration suppression · Parametric optimization

H. Lu · X. Wu (✉)
Institute of Intelligent Vehicles, Shanghai Jiao Tong University, Shanghai, China
e-mail: xiaodongwu@sjtu.edu.cn

G. Habib
Department of Applied Mechanics, Faculty of Mechanical Engineering, Budapest University of Technology and Economics, Műegyetem rkp. 3, Budapest 1111, Hungary

MTA-BME Lendület "Momentum" Global Dynamics Research Group, Budapest University of Technology and Economics, Műegyetem rkp. 3, Budapest 1111, Hungary

Y. Ren
School of Automotive and Transportation Engineering, Hefei University of Technology, Hefei, China

L. Yan
State Key Laboratory of Mechanical System and Vibration, Shanghai Jiao Tong University, Shanghai, China

1 Introduction

Advanced vehicle chassis is employing novel unsprung structures for better maneuverability and controllability, such as full-by-wire chassis [1] and independent in-wheel-motor (I-W-M) powertrain. Meanwhile, this also poses new challenges to the dynamic stability of each independent wheel with elastic tires [2,3], where within the upcoming problems, wheel shimmy becomes the primary vibration issue to be settled. Since the 1950s, the problem of shimmy in the classical vehicle steering column [4] and landing gears of aircraft [5] has received

Published online: 18 June 2024

wide attention, where researchers have generally concluded that shimmy is a typical nonlinear self-excited vibration induced mainly by the elastic tire properties and potential structural modal coupling [6,7]. It happens at a certain speed range with the appearance of supercritical Hopf bifurcations leading to the periodic oscillations of the wheel [8]. During shimmy, the kinetic energy of the forwarding speed, which is usually constrained as constant in dynamic models, is transferred to the oscillatory motion of shimmy. Shimmy appears as stable oscillations, which can have serious consequences when coupling with other vibration modes of the system; this effect is illustrated in [9,10], referring to vehicle lateral yawing or pitching, and in [11], regarding aircraft swaying and potential related accidents.

Shimmy problems are already dealt with in classical vehicles that are equipped with steering linkage or tie-rod connection in the early stages of the design and development of the steering system. By properly designing the structural parameters such as length or angles, and increasing the damping or stiffness within the steering column [12], the shimmy can be effectively prevented when coming into production. Nevertheless, shimmy could still reappear after a long mileage of services resulting from increased clearance of the steering rod [13], dry frictions [14], and loss of damping [15]. In advanced by-wire chassis, with the incorporation of novel unsprung structures and In-Wheel-Motor drive, each wheel subsystem forms up an individual domain with steering, driving torque, and suspension controlled locally to the high-level by-wire signals, thus making no mechanical connections between each other. Shimmy emerges from the weakened mechanical connection and the changed structural stability properties, and it is even harder to prevent by directly modifying the steer-by-wire control since its small and high-frequency characteristics carry different physical tasks. Generally, a tradeoff has to be made between the increase in subsystem mass and the decreased high-speed stability.

Recently, the utilization of active control methods to suppress wheel shimmy was proposed in the literature [16–18] and proved effective; however, it requires an extra actuator and control unit leading to difficulties in practical applications. The authors have also been engaging with such shimmy problems, and based on the acknowledgment of the successful applications of nonlinear energy sinks (NESs), the authors consider that it might be a good solution to suppress those shimmy problems for either developing vehicles or in-service vehicles, and these motivate the present study here.

An NES is a particular type of dynamic vibration absorber (DVA) consisting of a small mass attached to the main structure through a viscoelastic element. Unlike typical DVAs, which rely on a linear modal interaction with the primary system, the NES exploits a nonlinear restoring force to generate an amplitude-dependent natural frequency. This enables the NES to resonate in a broad frequency band, differently from classical DVA, which works only at a specific frequency [19,20]. In the last 20 years, the NES received growing attention from the scientific community, leading to many different designs [21]. These include the vibro-impact NES [22] (either double- or single-sided [23]), the rotary NES [24], the rotary-impact NES [25], the inerter-enhanced NES [26], the track NES [27], the bistable NES [28], the piecewise NES [29], the periodically extended NES [30], the softening NES [31], the unsymmetrical force NES [32] to name a few. In its classical design, the NES works fully passively and consists of a lightweight mass connected to the primary structure through a linear damper and a cubic spring [33]. Although alternative designs have better performance than the basic one, in this study, the basic NES design, with a single cubic spring, is considered. The reasons for this choice are the following: (i) the classical NES design provides more general results, which is convenient for a preliminary study as the present one; (ii) exotic designs are generally hard to be realized in practice [30]; (iii) vibro-impact NESs have a relatively simple design [34], but they are not a feasible option because of the generated noise. Accordingly, for the sake of simplicity, the authors adopt an ungrounded NES with a linear damper and a purely cubic spring.

The NES was implemented to mitigate impulsive [31,35], forced [36], self-excited [37,38], or parametric vibrations [39] in various applications, including aeroelastic instabilities [40], machine tool vibrations [38], seismic vibrations [41], to name a few. These studies exhibited promising results but also some limitations. In particular, differently from a linear DVA, the NES modifies the underlying linear system only marginally, making it ineffective for completely suppressing self-excited oscillations by enlarging the stability of equilibrium points [42,43]. Nevertheless, the NES can trigger quasi-periodic strongly modulated response with much lower amplitude than limit cycle oscillations (LCOs) of

the same system without NES, thus mitigating vibrations [37].

The idea of utilizing a DVA for suppressing shimmy instabilities is not novel; however, it is the first time that a DVA is employed in the wheel subsystem and the full body of typical grounded vehicles. In [44], a nonlinear tuned vibration absorber was implemented on a towed wheel. The considered DVA had a linear and a nonlinear restoring force and exhibited excellent performance. However, in that study, practical considerations about the size and required stroke of the absorber mass are omitted. In [45], the performance of an NES for mitigating shimmy oscillations of an aircraft landing gear was assessed. Results illustrate the efficiency of the NES, although potentially detrimental bistable behavior was also identified. Similar results were obtained in [46,47], utilizing a torsional NES also in an aircraft landing gear.

In this paper, the authors consider the feasible application of NES in a passenger vehicle to improve motion stability. Firstly, a single-wheel model is newly proposed to suit the requirement of a realistic and practical unsprung wheel system of vehicles. The effect of NES on linear stability and nonlinear dynamical behavior, especially regarding the oscillation amplitude and frequency, are discussed. Global parameter optimization is proposed to identify the best parameter set that minimizes the unstable speed range. Problems relative to robustness and multi-stability are also discussed, and in two new types of unsprung wheel systems, the effectiveness of the NES is verified. The key contributions of the paper are listed:

(1) based on the preceding success of NES in suppressing self-excited vibrations, the authors present a feasible way to passively control wheel shimmy by incorporating a lightweight NES structure into the advanced by-wire chassis of passenger vehicles, which, according to the authors' knowledge, was never proposed before.
(2) through the dynamic analysis of shimmy systems with NES, the authors conclude that an ungrounded NES structure is capable of suppressing the shimmy amplitude and mitigating the energy to a highly desired extent; meanwhile, the performance and robustness w.r.t the parametric uncertainties are examined and considered satisfying.
(3) the authors introduce a methodology for constructing a four-wheeled transient vehicle model by utilizing the single wheel system (SWS), and, by doing so, the performance of the NES on controlling the global vehicle motions is verified, which provides feasibility and functioning references for practical applications.

The rest of the paper is organized as follows. Section 2 establishes a SWS, and on this basis, the mechanism of shimmy appearance is analyzed. In Sect. 3, the NES structure is installed into the SWS, where the performance, robustness, and feasibility of the NES are presented and discussed. Section 4 further incorporates the SWS into a full vehicle to examine the suppression effect of the NES against the dynamic coupling between wheel shimmy and handling motions. Conclusions are summarized in the final part.

2 Dominant factors inducing wheel shimmy

For ground vehicles, shimmy can be induced by many factors, such as dry friction, clearance in the joint, heavy unsprung masses, etc, but fundamentally, the phenomenon of wheel shimmy occurs because of the tire-ground contact and structural parameters. In this section, the dominant factors contributing to typical wheel shimmy in ground vehicles are investigated, and an instructive single-wheel system (SWS) acquired from a quarter-car model is established as the basis.

2.1 Dynamic modeling of SWS

Figure 1 illustrates the mechanical model of the SWS in a locally fixed x, y, z coordinate system. Multiple geometric constraints are assumed, namely, (i) the kingpin is fixed to the imaginary vehicle body with only rotational motion allowed; (ii) the whole SWS is following the longitudinal speed of the vehicle u that is considered constant. Thus, the rotational angle θ of the wheel frame w.r.t the kingpin of the wheel frame is the only degree of freedom of the SWS. In Fig. 1c, the free body diagram of the SWS is presented and the corresponding dynamic model can be constructed easily by either Newtonian or Lagrangian methods. This reads

$$\begin{aligned}(J_{w,z}+m_w r^2)\ddot{\theta}(t)+(C_w+J_{w,y}\gamma\frac{u}{R})\dot{\theta}(t)\\ +(K_w+K_t R r\gamma^2)\theta(t)=-F_y\,(e+R\gamma)\ ,\end{aligned} \tag{1}$$

where $J_{w,z}$ and $J_{w,y}$ are the moment of inertia of the wheel evaluated at its center w.r.t to the axial direction

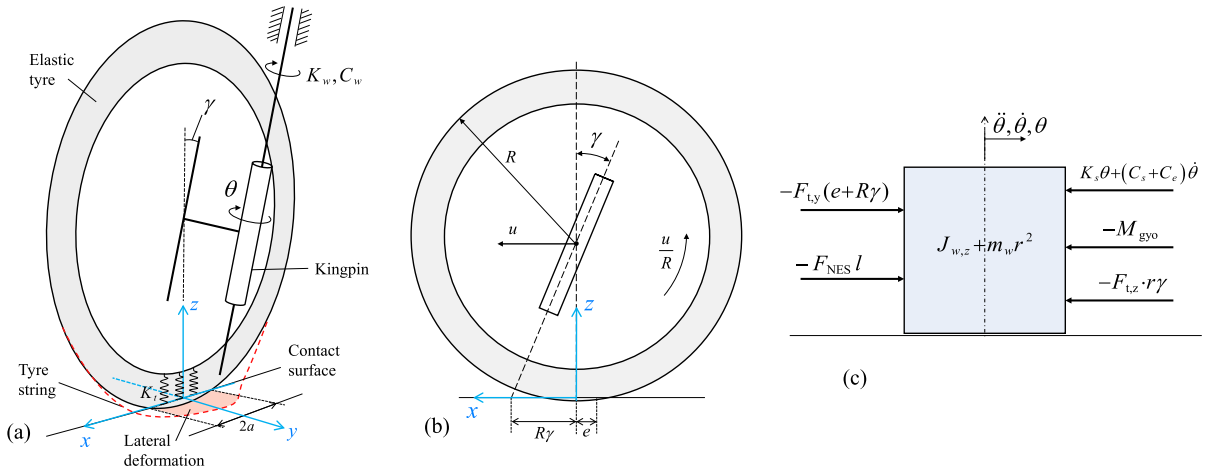

Fig. 1 SWS schematic model in **a** front view; **b** side view; **c** free body diagram

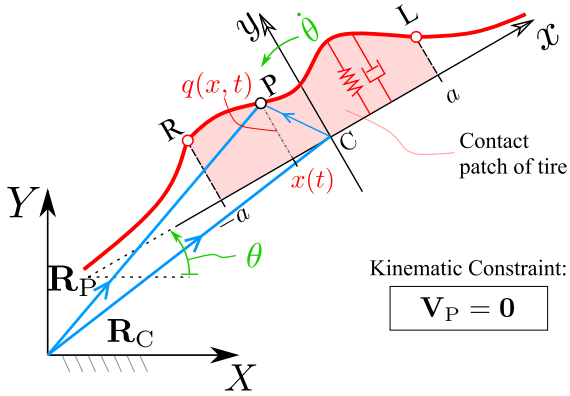

Fig. 2 Kinematic constraint of tire-ground contact points

z, y, respectively, m_w is the mass of the wheel, r is the lateral distance (y-axis) between the wheel center and the kingpin, R is the radius of the wheel, γ is the inclination angle of the kingpin, and K_w and C_w are the rotational stiffness and damping of the SWS w.r.t the kingpin.

Regarding the exerted forces, F_y denotes the tire lateral force generated from the tire-ground contact, and e is the pneumatic trail w.r.t the contact center, $F_{t,z} = -K_t R\gamma\theta$ is the vertical deflection forces of the tire due to the angular change of θ, and, finally, the gyroscopic moment $M_{gyo} = -J_{w,y}\gamma u/R$ due to wheel rotations is also included.

As seen in Fig. 1, the crucial part of the system lies in the tire-ground contact where strong nonlinearities are generated. To derive the law of contact motions, a kinematic constraint is incorporated, assuming that the tire particles are sticking to the ground without sliding. This is reasonable for small amplitude vibrations in the tires such as shimmy. On this basis, the stretched-string tire model is employed to describe the high-frequency vibrations in the tire contact (red line in Fig. 2). The kinematic constraint is described by $\mathbf{V}_P = \mathbf{0}$, that is $\dot{\mathbf{R}}_P = 0$, where P is one of the contact points in the stretched string. Regarding the earth-fixed coordinate system X, Y, Z (see Fig. 2), the kinematic constraint is derived as

$$\begin{aligned} \dot{X}_C + v\cos\theta - x\dot{\theta}\sin\theta - \frac{\mathrm{d}}{\mathrm{d}t}q\sin\theta - q\dot{\theta}\cos\theta = 0\,, \\ \dot{Y}_C + v\sin\theta + x\dot{\theta}\cos\theta - \frac{\mathrm{d}}{\mathrm{d}t}q\cos\theta - q\dot{\theta}\sin\theta = 0\,, \end{aligned} \tag{2}$$

where $q = q(x,t)$ is the lateral deflection of the tire string, and $v = v(x,t)$ is the translational speed of material point following $\dot{x} = v(x,t)$.

Simplification of (2) gives the partial differential equation (PDE):

$$\begin{aligned} \dot{q}(x,t) &= \dot{X}_C\sin\theta - \dot{Y}_C\cos\theta - x\dot{\theta} - q'(x,t)v(x,t)\,, \\ v(x,t) &= -\dot{X}_C\cos\theta - \dot{Y}_C\sin\theta - q(x,t)\dot{\theta}\,, \end{aligned} \tag{3}$$

where q' indicates the derivative with respect to x. For the stretched-string tire model, at the leading point of contact ('L' in Fig. 2), the boundary condition assumes (see [6])

$$q'(a,t) = -\frac{q(a,t)}{\sigma}\,,\ \alpha(t) = q'(a,t)\,, \tag{4}$$

where σ is the relaxation length, and substitution of (4) into (3) gives the kinematic relations in the form of

$$\dot{\alpha} = -\frac{\dot{X}_C}{\sigma}\theta + \frac{\dot{Y}_C}{\sigma} + \frac{a}{\sigma}\dot{\theta} - \frac{\dot{X}_C}{\sigma}\alpha\,, \tag{5}$$

while neglecting all the high-order terms, and in the case of the SWS where $\dot{X}_C = u$, $\dot{Y}_C = 0$, it equals to

$$\dot{\alpha} + \frac{u}{\sigma}\alpha = -\frac{u}{\sigma}\theta + \frac{a}{\sigma}\dot{\theta}\,. \tag{6}$$

With information on the contact at the leading edge, the Magic Formula [6] has good accuracy in approximating the total forces generated by the string (red line in Fig. 2) that reads

$$F_y(\alpha) = \mu F_z \sin\big(C\,(B\alpha - EB\alpha + E\arctan B\alpha)\big)\,, \tag{7}$$

where μ is the frictional coefficient, F_z is the vertical load, and B, C, E (given in Table 1) have no direct relation to physical properties. Their definition is provided in [6].

2.2 Stability analysis

Normalization of the SWS dynamics in Eqs. (1) and (6) is conducted to obtain the dimensionless parameters, as follows:

$$\begin{aligned} \frac{\mathrm{d}^2\theta}{\mathrm{d}t^2} + (\zeta + \zeta_1 u)\frac{\mathrm{d}\theta}{\mathrm{d}t} + \omega_n^2\theta &= -\omega_n^2 \upsilon\alpha\,, \\ \sigma\frac{\mathrm{d}\alpha}{\mathrm{d}t} + u\alpha &= a\frac{\mathrm{d}\theta}{\mathrm{d}t} - u\theta\,, \end{aligned} \tag{8}$$

where

$$\begin{aligned} &J_w = J_{w,z} + m_w r^2,\ \zeta = C_w/J_w,\ \zeta_1 = J_{w,y}\gamma/J_w R, \\ &\omega_n = \sqrt{\left(K_w + K_t R r\gamma^2\right)/J_w},\ \upsilon = K_y e/\left(J_w\omega_n^2\right), \end{aligned} \tag{9}$$

Note that K_y is the tire linear cornering stiffness acquired by multiplying $\mu F_z BC$.

Linear stability analysis for the trivial solution of Eq. (8) can be carried out by substituting the trial solution $\mathbf{x} = \mathbf{C}e^{\lambda t}, \mathbf{x} = [\theta, \alpha]^T$ that gives the characteristic function

$$D(\lambda) : \lambda^3 + a_2\lambda^2 + a_1\lambda + a_0 = 0\,, \tag{10}$$

where

$$\begin{aligned} a_0 &= \frac{1}{\sigma}\left({\omega_n}^2 u + {\omega_n}^2 u\upsilon\right),\ a_2 = \left(\frac{u}{\sigma} + \zeta + u\zeta_1\right), \\ a_1 &= \frac{1}{\sigma}\left(u\zeta + {\omega_n}^2\sigma + u^2\zeta_1 - a{\omega_n}^2\upsilon\right). \end{aligned} \tag{11}$$

The stability boundary are marked by eigenvalues crossing the imaginary axis to the positive side of the real axis. Accordingly, to find the stability limits, the boundary condition $\lambda = \mathrm{i}\omega$ is substituted into (10), and by splitting the results into the real part and imaginary part, the following equations are derived:

$$\begin{aligned} &\textbf{Re:} - a_3\omega^2 + a_1 = 0\,, \\ &\textbf{Im:} - \omega^3 + a_2\omega = 0\,. \end{aligned} \tag{12}$$

When $\omega = 0$, the static boundary is

$${\omega_n}^2 u(1+\upsilon) = 0\,, \tag{13}$$

meaning one real eigenvalue crosses the imaginary axis with no imaginary part. Such static loss of stability is related to a negative tire stiffness, which has obviously limited relevance in practice.

A more important case is when $\omega \neq 0$, and the stability loss is related to Hopf bifurcations. This occurs for the values of speed u and damping ζ:

$$\begin{aligned} u(\omega) &= \omega\sigma\sqrt{\frac{\Gamma(\omega)}{\sigma\,\Delta(\omega)}}\,, \\ \zeta(\omega) &= \frac{1}{\omega}\sqrt{\frac{\Gamma(\omega)}{\sigma\,\Delta(\omega)}}\,|\Delta(\omega) - \omega^2\sigma\zeta_1|, \end{aligned} \tag{14}$$

where

$$\begin{aligned} \Gamma(\omega) &= \omega^2\sigma - (a\upsilon - \sigma)\,{\omega_n}^2\,, \\ \Delta(\omega) &= \left({\omega_n}^2\upsilon - \omega^2 + {\omega_n}^2\right). \end{aligned} \tag{15}$$

Equation (14) provides real values only if $\Gamma(\omega)\cdot\Delta(\omega) > 0$. Considering Eq. (15), this is possible only when

$${\omega_n}^2\left(1 - \frac{a}{\sigma}\upsilon\right) < \omega^2 < {\omega_n}^2(\upsilon + 1). \tag{16}$$

Referring to the parameter values in Table 1, oscillation frequency varies in the interval $5.9 \sim 6.2$ Hz.

By exploiting Eqs. (10)–(14), the stability charts in the plane of system parameters are constructed in Fig. 3, where the shaded area 'S' denotes the stable regions and 'US' indicates the unstable ones, with Hopf bifurcations occurring on the boundaries. Factors inducing shimmy can be generalized as:

(1) longitudinal speed u has strong determinacy that restricts the existence of instability inside certain speed ranges as illustrated in each Fig. 3a, c.
(2) the rotational stiffness and damping of SWS can enlarge or shrink the instability ranges. This observation is consistent with previous results in the literature and common practices, where up-tuning of

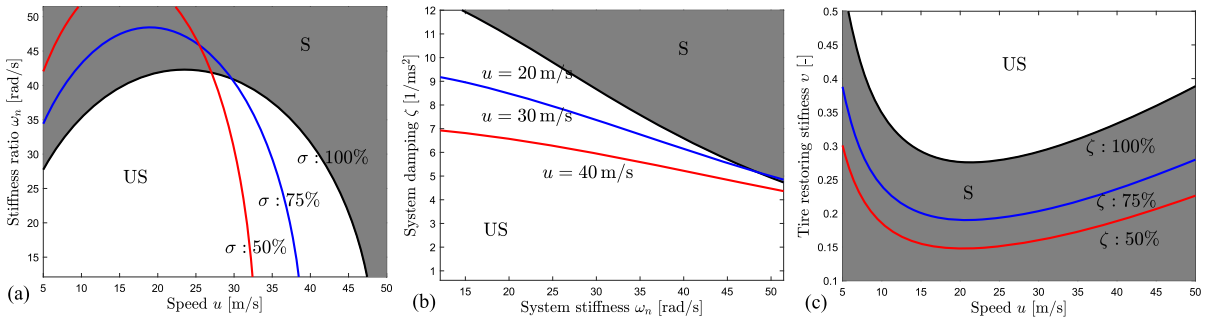

Fig. 3 Stability chart of the SWS at different parametric combinations, where 'US' denotes unstable parametric domains and 'S' indicates the stable ones. % indicates a percentage from parameters in Table 1

these two values is the advisable solution to avoid shimmy (e.g., steering damper in motorcycles and vehicles).

(3) one commonly neglected factor is the tire relaxation length σ that produce a non-negligible effect on the stability boundary. Its effect on unstable speed and stiffness ranges is shown in Fig. 3a.

2.3 Post-bifurcation behavior

Bifurcation diagrams of the SWS's dynamics are obtained through direct numerical simulations. They provide a reference against which the performance of the NES will be evaluated. In Fig. 4, the oscillation amplitude A_θ is represented for variations of the speed u and the relaxation length σ, where the damping ζ and stiffness ratio ω_n are encountered as the third factors.

In the nominal system parameters given in Table 1, the unstable region of the trivial solution is marked by the Hopf bifurcations at $u = 14$ m/s and $u = 33$ m/s, in accordance with the results of the stability chart in Fig. 3c. The effect of variations of the stiffness ratio ω_n and damping ratio ζ from their nominal values is provided by the colored lines.

3 Dynamic behavior of a SWS with an attached NES

In this section, the effectiveness of an NES for suppressing and mitigating shimmy oscillations of the SWS is evaluated. The linear stability and nonlinear dynamic behavior are investigated and NES performance is assessed with respect to the SWS studied in the previous section.

3.1 Stability analysis

The qualitative design for the NES, which encompasses a linear damper and a purely cubic spring, is depicted in Fig. 5. The whole structure is installed in the wheel frame, together with the ball joint to the steering and the pivots of the suspensions. Such installation carries no effect on either the balance of wheel rotations or the performance of the suspension.

The introduction of the NES brings an additional degree of freedom, marked by the NES lateral displacement $y(t)$. The coupling between the NES and the SWS is provided by elastic and damping terms proportional to their relative displacement and velocity. The equations of motion are

$$\begin{aligned} m_s\ddot{y}(t) &= -C_{\mathrm{NES}}\left(\dot{y}(t) - l\dot{\theta}(t)\right) \\ &\quad - K_{\mathrm{NES}}\Big(y(t) - l\theta(t)\Big)^3, \\ J_w\ddot{\theta}(t) &= -(C_w + J_{w,y}\gamma\frac{u}{R})\dot{\theta}(t) \\ &\quad - (K_w + K_t R r\gamma^2)\theta(t) \\ &\quad - F_y(e + R\gamma) - F_{\mathrm{NES}}l, \end{aligned} \tag{17}$$

where l is the control arm length, and the feedback force F_{NES} is

$$\begin{aligned} F_{\mathrm{NES}} &= C_{\mathrm{NES}}\left(\dot{y}(t) - l\dot{\theta}(t)\right) \\ &\quad + K_{\mathrm{NES}}\Big(y(t) - l\theta(t)\Big)^3. \end{aligned} \tag{18}$$

Equations (17) and (6) function as the basis for numerical simulations.

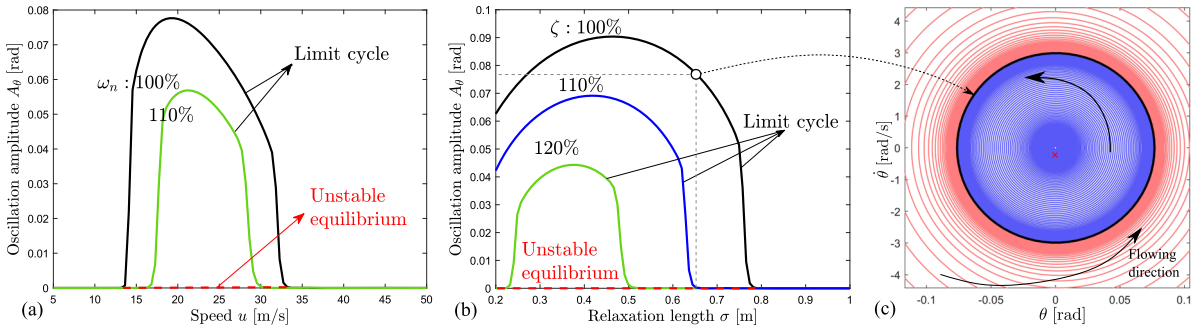

Fig. 4 Bifucation amplitude of the SWS at **a** different longitudinal speed u and stiffness ω_n and **b** different relaxation length a and damping ratio ζ, respectively, where panel **c** represents the phase plane corresponding to the limit cycle oscillation (solid line)

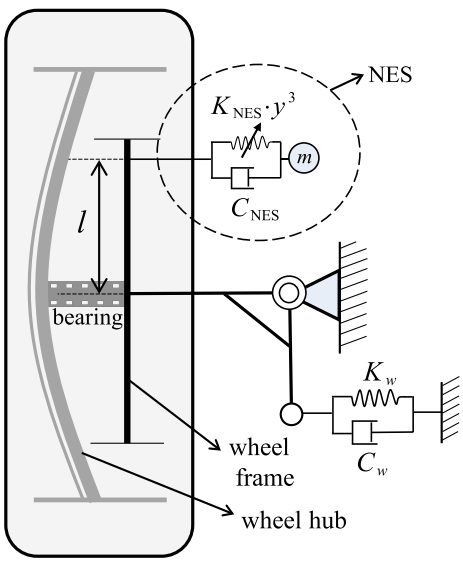

Fig. 5 Mechanical model of the NES installation in the SWS

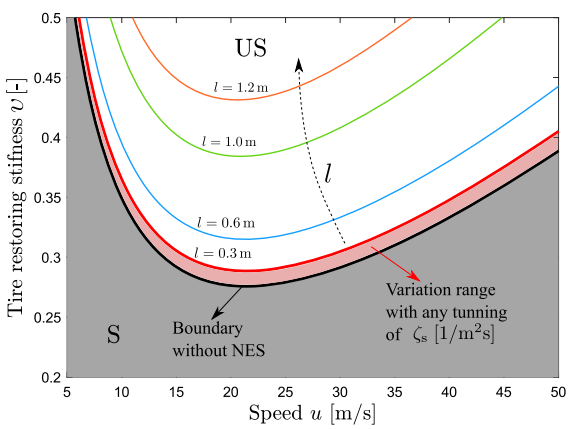

Fig. 6 Stability chart of the SWS with NES installed at different parameter configurations

Similarly to the case of only the SWS, normalization is conducted, providing

$$\begin{aligned}
&\frac{\mathrm{d}^2\theta}{\mathrm{d}t^2} + (\zeta + \zeta_1 u)\frac{\mathrm{d}\theta}{\mathrm{d}t} + \omega_n^2\theta = \\
&\quad -\omega_n^2\upsilon\alpha + \eta\zeta_s\left(\frac{\mathrm{d}\theta}{\mathrm{d}t} - \frac{1}{l}\frac{\mathrm{d}y}{\mathrm{d}t}\right) + \eta\omega_s^2\left(\theta - \frac{y}{l}\right)^3 \\
&\frac{\mathrm{d}^2 y}{\mathrm{d}t^2} + \zeta_s\left(\frac{\mathrm{d}y}{\mathrm{d}t} - l\frac{\mathrm{d}\theta}{\mathrm{d}t}\right) + \omega_s\,(y - l\theta)^3 = 0
\end{aligned} \tag{19}$$

where

$$\eta = m_s l^2/J_w,\ \zeta_s = C_{\mathrm{NES}}/m_s,\ \omega_s = \sqrt{K_{\mathrm{NES}}/m_s}. \tag{20}$$

Following the procedure utilized for the SWS, the stability is analyzed through the characteristic function, which reads

$$D_s(\lambda) : \lambda\left(\lambda^4 + a_3\lambda^3 + a_2\lambda^2 + a_1\lambda + a_0\right) = 0\,, \tag{21}$$

where

$$\begin{aligned}
a_3 &= \left(\frac{u}{\sigma} + \zeta_s + \zeta + \eta\zeta_s + u\zeta_1\right)\,, \\
a_2 &= \frac{1}{\sigma}\Big(u\zeta_s + u\zeta + {\omega_n}^2\sigma + u^2\zeta_1 - a{\omega_n}^2\upsilon \\
&\quad +\eta\sigma{\zeta_s}^2 + \eta u\zeta_s + \sigma\zeta_s\zeta + \sigma u\zeta_1\zeta_s\Big)\,, \\
a_1 &= \frac{1}{\sigma}\Big({\omega_n}^2 u - \eta\sigma{\zeta_s}^2 + \eta u{\zeta_s}^2 + {\omega_n}^2 u\upsilon \\
&\quad +{\omega_n}^2\sigma\zeta_s + u^2\zeta_1\zeta_s + u\zeta_s\zeta - a{\omega_n}^2\upsilon\zeta_s\Big)\,, \\
a_0 &= \frac{1}{\sigma}\left({\omega_n}^2 u\zeta_s - \eta u{\zeta_s}^2 + {\omega_n}^2 u\upsilon\zeta_s\right)\,,
\end{aligned} \tag{22}$$

Note that since the system has no linear stiffness, a central manifold $\lambda = 0$ exists in the dimension of the

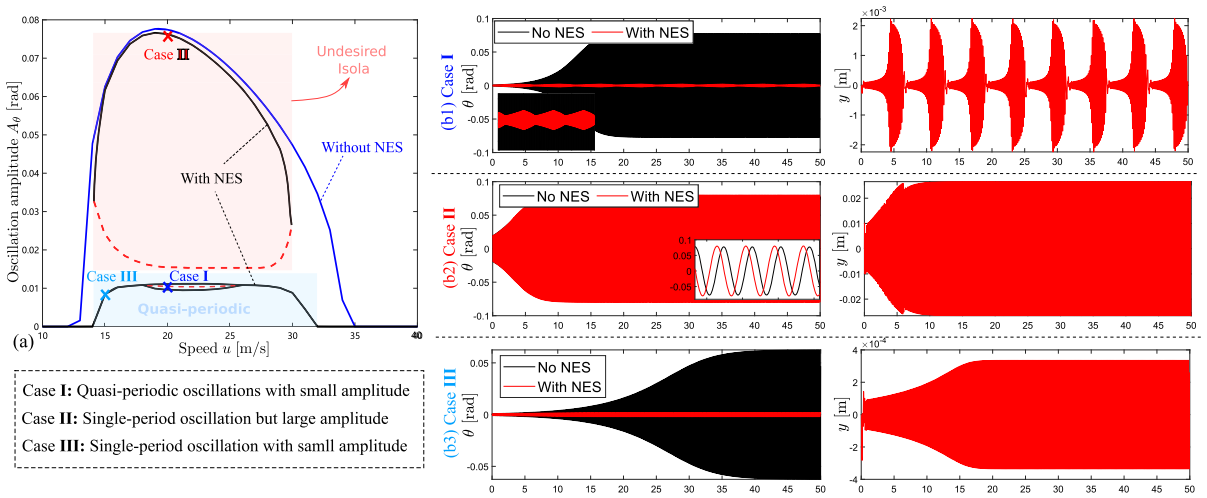

Fig. 7 Bifurcation characteristics of the SWS with NES installed. **a** bifurcation diagram using shimmy angular amplitude; **b1–b3** time-domain histories of shimmy angular responses and NES displacements in three cases, respectively

NES displacement, which is not stable in the linearized sense, but stable in the global sense. Methods like the Routh-Hurwitz criterion or eigenvalue calculation can be implemented here to derive the boundary of stability, and here for simplicity, the analytical result is derived by the symbolic calculation in Mathematica and is not listed.

Figure 6 plots the resulting stability chart of the original SWS and the one with NES. Before the analysis, several parameters of NES have to be clarified. The length of the NES arm is geometrically constrained within the wheel hub, which reasonably follows $l \leq 0.3$ m in our case. As a general rule, the larger the NES mass, the better its performance is; however, practical considerations usually limit its value. In this case, the maximal NES mass is set to 1 kg. Conversely, the total unsprung mass m_w of the wheel is relatively heavy for an I-W-M driven vehicle and it is set to 30 kg. All these practical constraints significantly limit the value of the moment of inertia ratio η, which is proportional to the coupling force between the NES and the wheel.

With NES parameters selected in the above range, variation of the corresponding stability chart of the system is presented in the red shadowed region of Fig. 6, in which the tuning of the damping coefficient has little effect on the linear stability of the system compared with original SWS. While if the constraint on the length of the NES arm is neglected by further increasing l, Fig. 6 indicates that the stability boundary is modified in a much extensive range. The limited effectiveness of the NES for enlarging the stable region is due to its lack of a linear restoring force term, which significantly restricts its significance for linear stability, as previously illustrated in [42], for example. This outcome is consistent with results obtained in [37] for the suppression of flutter instabilities.

The authors note that a classical linear DVA would significantly outperform the NES in terms of linear stability, as illustrated for example in [44]. Nevertheless, the DVA has strict tuning requirements and has a limited effect on vibration amplitude when instabilities are triggered. In any case, a detailed comparison between the DVA and NES performance for shimmy suppression is beyond the scope of this paper.

3.2 NES performance in the nonlinear regime

To check the performance of the NES in the shimmy suppression and passive energy transfer, the nonlinear analysis focusing on the bifurcations, vibration amplitude, and dynamical behavior is conducted through numerical simulations and calculations.

3.2.1 Preliminary procedure to locate the effective parameter domain of NES

The initial setup of NES parameters is always challenging for designers since several modifiable parameters of NES are not constrained, and meanwhile, one should

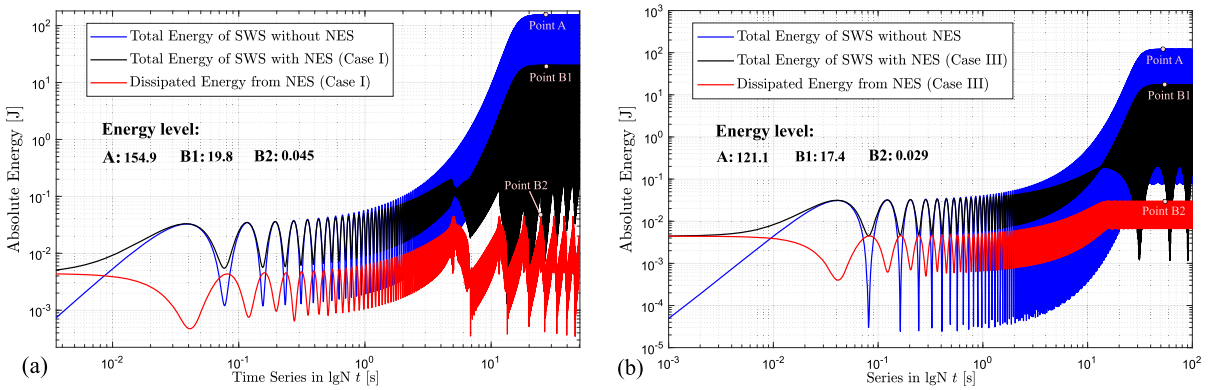

Fig. 8 Comparison of mechanical and dissipated energy in the SWS without and with NES installed, respectively. The calculated energy corresponds to (a) Case I in Fig. 7(b1), and (b) Case III in Fig. 7(b3)

only focus on the effective part of the parameters of the NES to study its consequent performance. Thus, the authors propose a judgment criterion here for assessing the performance of the NES based on the relative energy ratio, i.e.,

$$\epsilon = \frac{\sum_{k=1}^{n_1} |A_{\text{nes}}(t_k)|/n_1}{\sum_{l=1}^{n_2} |A_{\text{sws}}(t_l)|/n_2}, \tag{23}$$

where $A_{\text{nes}}(t_k)$ and $A_{\text{sws}}(t_l)$ are the peaking points collected from the discrete vibrational signal of $\theta(t_m)$, $m \in \mathbb{Z}$ following

$$\begin{aligned} &\text{if } |\theta(t_m)| > \max\{|\theta(t_{m-1})|, |\theta(t_{m+1})|\}, \\ &\text{then } A_{\dots}(t_k) = \theta(t_m)\,, \end{aligned} \tag{24}$$

and n_1, n_2 count the overall number of amplitude A. Physically, ϵ represents the energy ratio evaluated by the size of the averaged amplitudes of oscillations when the system settles to steady-state conditions.

According to this criterion, a global searching algorithm based on Matlab 'fminsearch' function is implemented to locate the parameter region with the smallest energy ratio ϵ.

The optimization is performed for a fixed velocity of $u = 20$ m/s, fixing $m_s = 1$ kg and $l = 0.3$ m. It provided a minimal $\epsilon_{\min} = 0.09$ for the parameter values $\omega_s \approx 2.4 \times 10^4\, 1/(\text{m s})$ and $\zeta_s = 9\, 1/(\text{m}^2\,\text{s})$. Figure 7(b1) (Case I) presents the dynamical responses corresponding to the derived NES parameters, and, as the signal comparison indicates, the SWS with NES installed indeed has significantly smaller vibrations but the oscillations are dynamically modulated: the

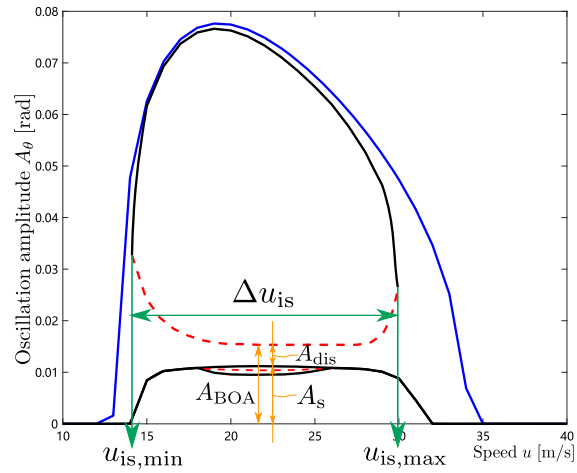

Fig. 9 Optimization targets visualized in the bifurcation diagrams: (1) reduce the Isola's range of appearance; (2) enlarge the domain of attraction for quasi-periodic oscillations

NES continuously absorbs the energy but also periodically modulates the amplitude and frequency. The $\epsilon_{\min} \approx 0.09$ represents an averaged amplitude ratio in quasi-periodic oscillations. According to practices of NES in literature, such signal modulation process proves the effective functioning of NES.

3.2.2 Global dynamics under NES modulations

The obtained solution, although extremely promising with respect to the NES performance, does not rule out that other solutions, less effective, can coexist with it. This occurrence can be verified through a global analysis. Direct numerical calculation is carried out to

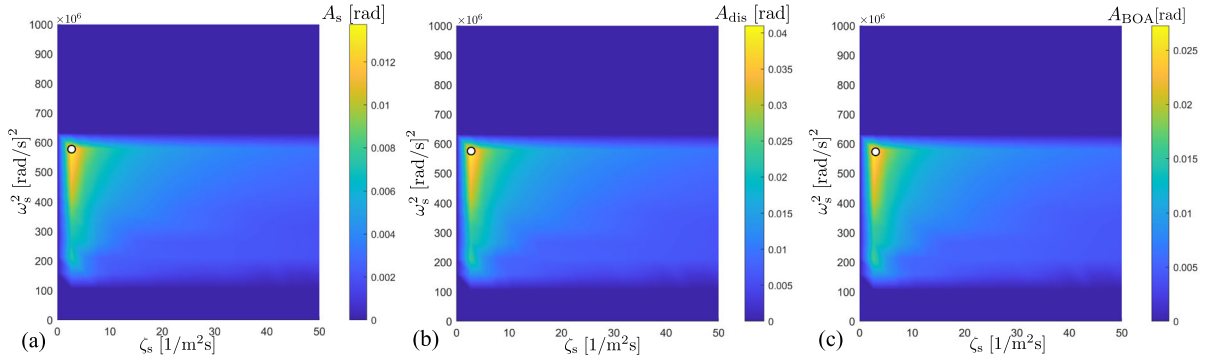

Fig. 10 Mapping of NES stiffness and damping to the size of domian of attraction of the desired oscillations, where the absolute amplitude A_s, relative distance to Isola A_{dis}, and the range of attracted domain A_{BOA} are incorporated into optimization

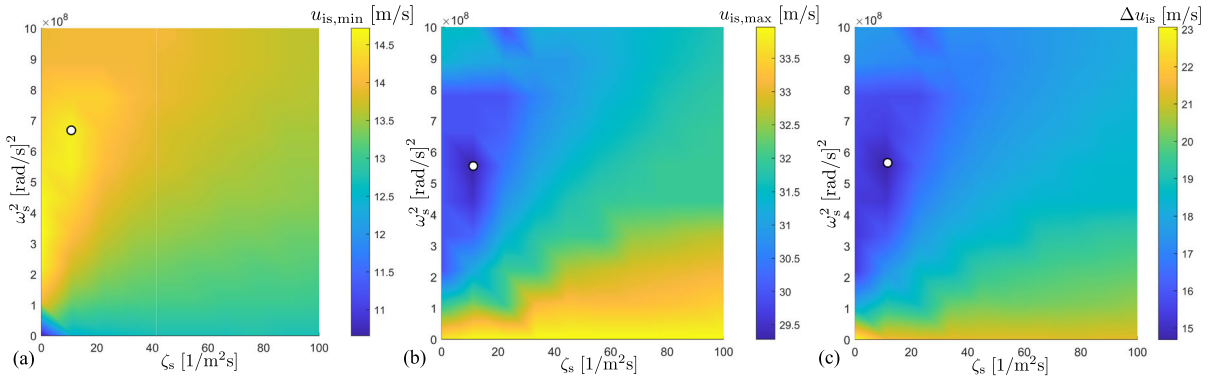

Fig. 11 Mapping of NES stiffness and damping to the range of appearance of the undesired Isola, where the lower boundary $u_{is,min}$, upper boundary $u_{is,max}$, and the relative range Δu_{is} are incorporated into optimization

locate different steady-state oscillations of the system under different initial conditions.

Figure 7a plots the bifurcation diagram of the SWS both with and without NES. The bifurcation parameter in the x-axis is the speed u, while the y-axis indicates the steady-state shimmy amplitude A_θ. The black solid line refers to the calculated stable LCO(s) with the NES, where the upper one shows a single-period LCO oscillation, while the lower lines denote the quasi-periodic oscillations. Compared with the bifurcation amplitude of the SWS without NES (blue solid line), the lower quasi-periodic oscillations are the desired vibrational responses that are also demonstrated by the energy ratio $\epsilon \approx 0.09$. Conversely, the upper LCO has generally little difference from the system without NES, indicating the ineffectiveness of NES in this regime. The fact that two stable solutions coexist, one effective and the other ineffective with respect to the NES performance, makes it important to evaluate their dynamical integrity and basin of attraction to correctly assess the effectiveness of the NES.

Figure 7 illustrates the time series of three different identified motions. Figure 7b1 refers to the modulated response, discussed above (Case I). Figure 7b2 depicts the time series of a poorly performing case, with large shimmy oscillations (Case II). Finally, Fig. 7b3 shows another priodic motion, also with excellent performance, obtained for a different value of the speed u (Case III). Different initial conditions lead the system to one of these cases. Note that Case III does not coexist with Case I, but only with Case II.

The mechanical and dissipated energy of the SWS is plotted in Fig. 8 where systems with and without NES are compared under the same instantaneous input energy, respectively. In both cases, NES is functioning well which reduces the total energy to an approximated 10% level. To compare, in the early responses of Case I in Fig. 8a, the SWS with NES shows smaller

energy fluctuations and at a certain stage, NES cut off the rising tendency of total energy in the SWS, where the system enters steady-state conditions. Case III in panel (b) presents similar early-stage phenomenons, while the suppressing process is smoother than Case I, and exhibits only single-period energy fluctuations in steady-states.

3.2.3 Analysis of the unstable solution

The dynamical integrity of the highly-performing solutions (Case I and III) can be estimated through their basins of attraction; however, entirely obtaining them is computationally expensive. So, only a 1-D section of the basin of attraction is computed, limited to the variable θ, and the whole range of speed u is considered within the calculation. This approach provides a reasonable estimation of the dynamical integrity at a limited computational cost, although with some uncertainty.

The boundary of the basins of attraction of the low and high amplitude solutions along θ is computed through a bisection method in the following steps:

(S-1) set initial condition $\theta_u(0) = A_{\text{ub}}$ from large stable LCO and $\theta_l(0) = A_{\text{lb}}$ from quasi-periodic oscillation;
(S-2) calculate the steady-state vibration A_{avg} at initial condition $\theta_l(0) = (A_{\text{ub}} + A_{\text{lb}})/2$, and identify the one with different amplitude to A_{avg};
(S-3) update A_{ub} and A_{lb} using the identified one and A_{avg} based on their values. Then, repeat the process until reaching the desired accuracy.

Through this procedure, a point of the boundary of the basins of attraction of the two solutions for each speed u value was located, as illustrated in Fig. 7a (red dotted line). The procedure does not guarantee that the identified point is the closest boundary to the small amplitude solution in the θ direction; however, the obtained curve suggests that the identified value and its distance from the stable solutions are strictly related to their dynamical integrity. The red line, together with the branch of high-amplitude periodic solutions, forms an isola of LCOs.

In view of the observed global dynamics, the lower quasi-periodic solution is the desired one, thus, it is important to optimize the system dynamics also with respect to the branch of isolated solutions (Isola) and offers maximal robustness against external excitations (dynamical integrity) of the lower stable solution.

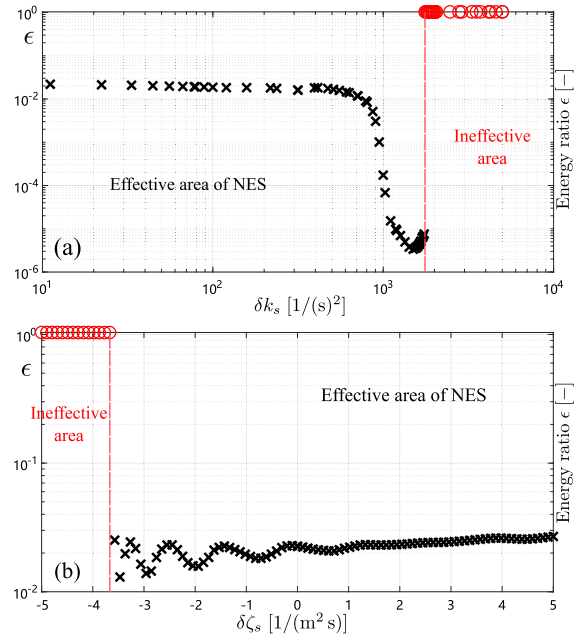

Fig. 12 Parametric robustness of the NES w.r.t **a** linear damping and **b** linear stiffness uncertainties appearing in practice

3.3 Optimization with respect to global dynamics

To improve the robustness and functional range of the NES system, another optimization is performed concerning the identified system's global dynamics. The main objective of the optimization is to find the absorber parameters which minimize the shimmy amplitude, reduce the velocity range where the isola exists, and maximize the robustness of the low-amplitude solution. Figure 9 labels the optimization targets explained as follows: Δu_{is} measures the speed range of the existing Isola, and $u_{\text{is,min}}, u_{\text{is,max}}$ are the corresponding minimum and maximum boundary value of speed; A_{BOA} assesses the estimated domain of attraction of the desired vibrations, while A_{S} evaluates the performance of the NES in energy absorption and A_{dis} denotes the distance to the boundary of basin of attraction.

The optimization is performed based on the proposed method in analyzing the global dynamics at various speeds in Fig. 7. For the robustness optimization, the speed is kept at $u = 20$ m/s, and by sweeping the

whole possible domain of ω_s and ζ_s, the optimal parameter configurations in the plane of ω_s and ζ_s can be identified.

The optimization results are presented in Figs. 10 and 11. Interestingly, six panels with different optimization quantities nearly show the same optimal value for the nonlinear stiffness that is $\omega_s^2 \approx 556 \times 10^6\, 1/(\mathrm{m\,s})^2$, even in Fig. 11a, a little shift carried bare difference in the resulting performance. In case of linear damping ratio ζ_s, consistency only holds for optimization in the same groups, where Fig. 10 calculates the optimal value at $\zeta_s = 3.9\, 1/(\mathrm{m}^2\,\mathrm{s})$, while Fig. 11 provides the optimal with $\zeta_s = 12.0\, 1/(\mathrm{m}^2\,\mathrm{s})$. Further observation of the corresponding effect of two optimal values in the counter groups indicates that a trade-off between the domain of attraction of quasi-periodic oscillation and the size of the Isola has to be determined, which also imposes limitations on the NES performance in designing.

3.4 Parametric robustness for NES performance

Referring to real-world applications, mechanical systems always have part of linear stiffness/damping that cannot be eliminated and such a condition is also unavoidable in the NES installation. It remains a crucial question about the functioning and tolerance range of NES against different types of parametric uncertainties. Thus, in this section, the effect of non-zero linear stiffness (denoted as δk_s) and tolerance range of damping uncertainties (denoted as $\delta\zeta_s$) on the prescribed performance of the proposed NES structure is investigated. Consequently, the feedback and transferring NES force is modified as

$$\widetilde{F}_{\mathrm{NES}} = F_{\mathrm{NES}} + m_s \delta k_s e_y + m_s \delta\zeta_s \dot{e}_y\,, \tag{25}$$

where $e_y = y - l\theta$.

Figure 12 presents the calculated results evaluated by the index of energy ratio ϵ in (23). In panel (a), at the range of $\delta k_s < 10^3\ 1/s^2$, the corresponding energy ratio stays steady, and further increase of δk_s even suppress the shimmy amplitude even more. When a critical boundary $\delta k_s < 1.75 \times 10^3\ 1/s^2$ is breached (red dotted line), NES suddenly loses all the designed performance and becomes ineffective due to the merging of the Isola and the stable lower amplitude solution leaving only the upper LCO. However, this critical value is relatively large meaning the designed NES is functional even with assembly errors in stiffness.

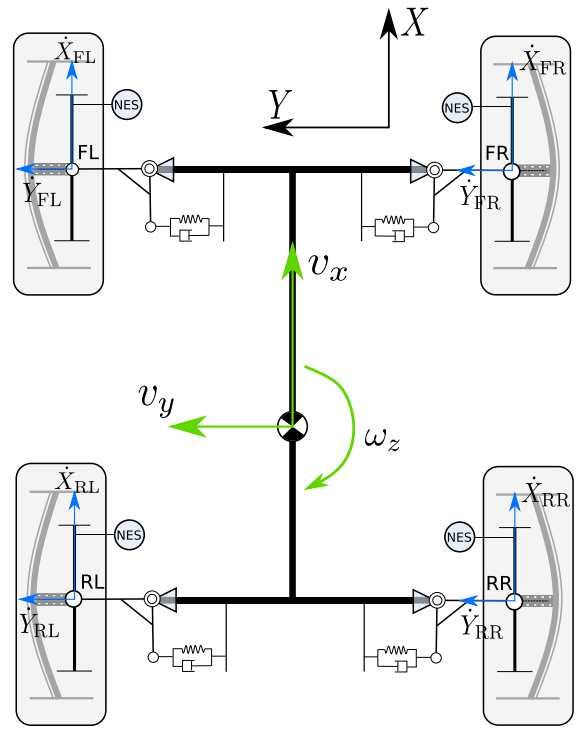

Fig. 13 Integration of the SWS with NES into the dynamic model of the full vehicle

Panel (b) plots the resulting performance of NES w.r.t the uncertainties in the damping coefficients, where $\delta\zeta_s$ is set to be varying between -5 to $5\ 1/(\mathrm{m}^2\,\mathrm{s})$. Accordingly, the energy suppression keeps steady variations between $(-3.7, 5)$, while in the case of greatly decreased $\delta\zeta_s$ crossing the critical boundary, total loss of performance is observed. Nevertheless, this range is also satisfactory since the original damping coefficient is $\zeta_s = 9\, 1/(\mathrm{m}^2\,\mathrm{s})$, thus almost 40% of parametric robustness is guaranteed.

4 Application and effectiveness of NES in four-wheeled vehicle systems

In ground vehicles with more than one wheel, the phenomenon of shimmy is also strongly related to the dynamic couplings between the steering shimmy and the kinematic motions of the vehicles itself. Such coupling could be further enlarged with the incorporation of the I-W-M and independent steering. However, modeling the global dynamics of the vehicle that includes the steering wheel shimmy is always highly complex

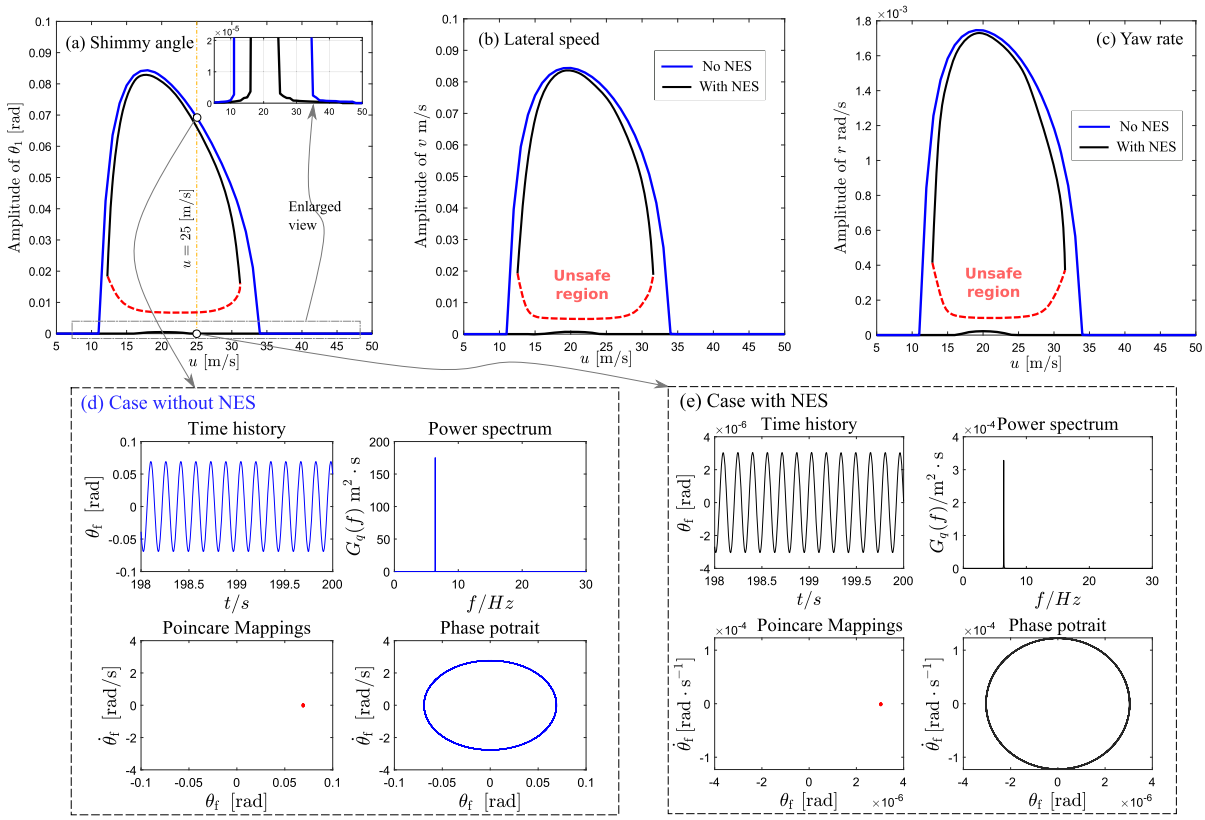

Fig. 14 Bifurcation characteristics of FVM with NES. **a–c** Bifurcation diagram of front wheel shimmy angle, lateral speed, and yaw rate of the vehicle body; **d**, **e** time history, power spectrum, Poincare mapping, and phase planes of FVM without and with NES installed, respectively

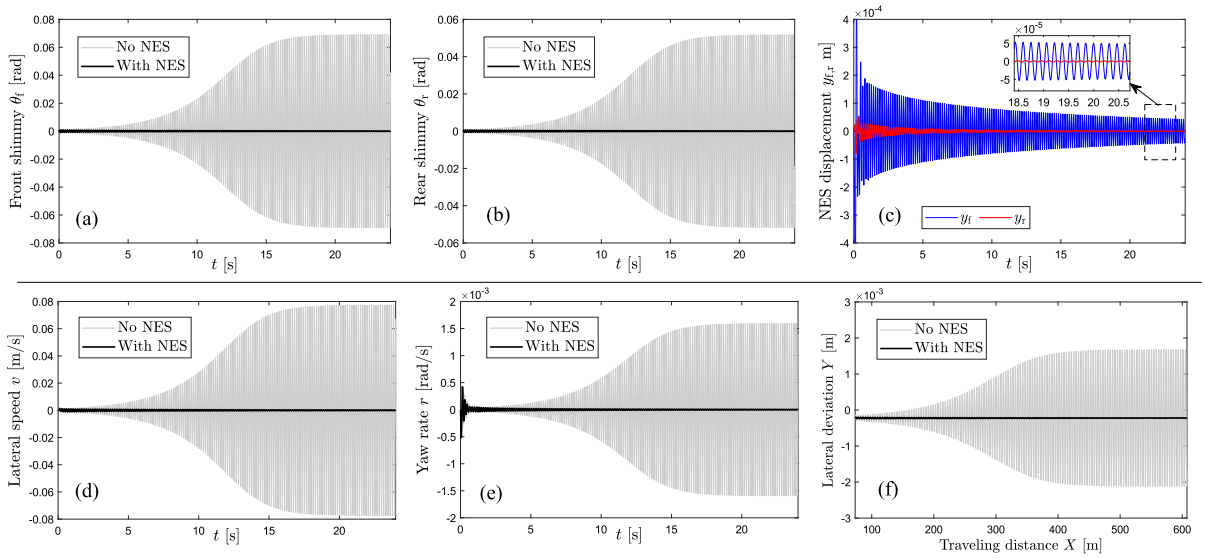

Fig. 15 Times history comparison in the status of **a–c** wheel shimmy and **d**, **e** lateral handling motions of FVM with and without NES

as shown in [48,49], due to many contributing degrees of freedom. In this section, a simple but instructive approach to model the full vehicle dynamics coupled with shimmy in direct integration of the SWS is provided. By doing so, the analysis of NES performance on vehicle motion can be quickly investigated.

4.1 Incorporating SWS into four-wheeled vehicles

Figure 13 sketches the full vehicle model (FVM) with NES equipped, where the coordinate is defined consistently as in Fig. 1. The longitudinal speed of the vehicle is assumed to be constant, i.e., $v_x \equiv u$. Kinematically, the interacted link between the body motions and shimmy motions is the velocity in the contact center of the wheels, which is described by $\dot{X}_i, \dot{Y}_i, i \in \{\mathrm{FL}, \mathrm{FR}, \mathrm{RL}, \mathrm{RR}\}$ for each wheel in Fig. 13. These velocities can be easily acquired through kinematic relations that read

$$\begin{aligned} \dot{X}_{\mathrm{FL}} &= \dot{X}_{\mathrm{FR}} = v_x - d_T \omega_z \,, \\ \dot{X}_{\mathrm{RL}} &= \dot{X}_{\mathrm{RR}} = v_x + d_T \omega_z \,, \\ \dot{Y}_{\mathrm{FL}} &= \dot{Y}_{\mathrm{FR}} \approx v_y + l_{\mathrm{f}} \omega_z \,, \\ \dot{Y}_{\mathrm{RL}} &= \dot{Y}_{\mathrm{RR}} \approx v_y - l_{\mathrm{r}} \omega_z \,, \end{aligned} \tag{26}$$

where $l_{\mathrm{f}}, l_{\mathrm{r}}$ are the distance from the center of gravity to front and rear axles, respectively, d_T is half-track width. With a generalized form of tire constraint equation in (5), equations for the transiency of each tire can be derived by substituting (26) into (5):

$$\begin{aligned} \dot{\alpha}_{\mathrm{f}} + \frac{u}{\sigma}\alpha_{\mathrm{f}} &= +\frac{1}{\sigma} v_y + \frac{l_{\mathrm{f}}}{\sigma}\omega_z - \frac{u}{\sigma}\theta_{\mathrm{f}} + \frac{a}{\sigma}\dot{\theta}_{\mathrm{f}} \,, \\ \dot{\alpha}_{\mathrm{r}} + \frac{u}{\sigma}\alpha_{\mathrm{r}} &= \frac{1}{\sigma} v_y - \frac{l_{\mathrm{r}}}{\sigma}\omega_z - \frac{u}{\sigma}\theta_{\mathrm{r}} + \frac{a}{\sigma}\dot{\theta}_{\mathrm{r}} \,, \end{aligned} \tag{27}$$

where due to indifference between the left and right side wheel, $\alpha_{\mathrm{f}}, \theta_{\mathrm{f}}$ and $\alpha_{\mathrm{r}}, \theta_{\mathrm{f}}$ with $\mathrm{f} = \mathrm{FL}, \mathrm{FR}, \mathrm{r} = \mathrm{RL}, \mathrm{RR}$ are employed to describe the tire sideslip angle and shimmy angle in the front and rear axle, respectively.

On the basis of the planar assumption, the equations of motions for the FVM with the NES are listed:

$$\begin{aligned} \dot{v}_y &= \frac{1}{m_v}\left(\sum F_{y,i}\right) - v_x \omega_z \,, \\ \dot{\omega}_z &= \frac{1}{J_v}\left(\left(F_{y,\mathrm{FL}} + F_{y,\mathrm{FR}}\right) l_{\mathrm{f}} - \left(F_{y,\mathrm{RL}} + F_{y,\mathrm{RR}}\right) l_{\mathrm{r}}\right) \,, \end{aligned} \tag{28}$$

where m_v, I_v are the total mass and inertia of the vehicle given in Table 1, respectively, and $F_{y,i}$ denotes the tire lateral forces calculated by substituting the following α_i into (7). The parametric data of the vehicle in Table 1 is collected from a B-class full-by-wire test vehicle with independent steering subsystems.

Table 1 Parameter values of SWS (upper) and FVM (lower)

$m_w = 30\,\mathrm{kg}$	$J_{\mathrm{w,z}} = 6\,\mathrm{kg\,m^2}$	$J_{\mathrm{w,y}} = 1.5\,\mathrm{kg\,m^2}$
$C_w = 36\,\mathrm{N\,s/m}$	$K_w = 8820\,\mathrm{N\,m}$	$K_t = 40,000\,\mathrm{N\,m}$
$\sigma = 0.6\,\mathrm{m}$	$a = 0.2\,\mathrm{m}$	$e = 0.1\,\mathrm{m}$
$\gamma = 0.04\,\mathrm{rad}$	$R = 0.36\,\mathrm{m}$	$r = 0.06\,\mathrm{m}$
$m_v = 1230\,\mathrm{kg}$	$J_v = 2150\,\mathrm{kg\,m^2}$	$l_{\mathrm{f,r}} = 1.3\,, 1.5\,\mathrm{m}$
$B = 13$	$C = 1.2$	$E = -1$

The associated kinematics for calculating the absolute position of the vehicles read

$$\begin{aligned} \dot{X} &= v_x \cos\psi - v_y \sin\psi, \\ \dot{Y} &= v_x \sin\psi + v_y \cos\psi \,, \\ \dot{\psi} &= \omega_z \,, \end{aligned} \tag{29}$$

where X, Y denote the positions in the absolute coordinate, and ψ gives the heading angle.

Combining equations (27), (28), and (29) with four SWS models for each wheel as listed in (1), the global dynamic model of the FVM can be derived. In this paper, the authors consider all four wheels to be independently steerable, thus all four subsystems of wheels are modeled. The parameters of this FVM are given in Table 1.

4.2 Effect of NES on improving handling stability

Based on the proposed FVM, the authors analyze the NES effect both on the stability of shimmy and handling motions, and the results are presented in Figs. 14 and 15.

Panel (a-c) in Fig. 14 demonstrates that without NES, wheel shimmy appears accompanied by periodic oscillations in the lateral speed and yaw rate of the vehicle body, due to the kinematic couplings in the tire transiency. This consequently leads to an unstable lane-keeping behavior as shown in the time histories of absolute positions of the vehicle in Fig. 15f, which is clearly undesirable even at a small amplitude.

The incorporation of the NES shows a promising result for the FVM system, where both the dynamic and kinematics state oscillation amplitudes are significantly mitigated (see black solid line in Figs. 14a–c

and 15). The characteristics of the dynamic responses of the FVM follow Case III in Fig. 7 with no modulation processes but only one stable LCO, which demonstrates the NES installation in the FVM has reduced the quasi-periodic oscillation into a single-periodic one.

Even though the vibration amplitude of the LCOs is extremely close to 0, linear stability is barely changed with NES installed, which can be observed by comparing the intersected points of two curves with horizontal axis in the enlarged panel of Fig. 14a. This can be further verified by comparing panels (d) and (c) in Fig. 14, where similarly shaped LCOs appear at the same oscillation frequency. Meanwhile, the independent Isola still exists above the stable LCO restricting the robustness of the NES with respect to state perturbations. Such limitations also hold for state variables of vehicle motions where the unsafe regions (red marked) indicate the critical boundary.

Checking the time histories of NES vibrations, it can be found that the NES installed in the front wheels has a larger amplitude of vibrations than the NES in the rear wheels, and conversely, in cases without NES, the rear wheel exhibits a larger shimmy angle. This is traced to the difference in the front and rear tire formulas as in (26) and also, to the steering characteristics of the vehicle determined by the ratio of l_f to l_r.

5 Conclusion

In this paper, the application of NES to suppress shimmy instability of vehicle motions is investigated, where the results in aspects of bifurcation, energy absorption, and robustness demonstrate that the installation of NES has great potential in improving the motion stability for advanced vehicle chassis design. The main conclusions are listed:

(I) The proposed SWS model from a quarter vehicle shows eminent effectiveness in analyzing the wheel shimmy phenomenon. Utilization of the SWS straightforwardly exposes the dominant factors inducing shi-mmy from delay effects in tire side-slip to the structural parameter designs.

(II) Installation of NES has little influence on the linear stability of SWS, unless with an unrealistic setup of parameters. However, NES achieves promising performances in the nonlinear range by suppressing and reducing oscillation amplitude up to 90%.

(III) In conditions of large state perturbation, intricacy is exhibited in the bifurcation diagram notifying the existence of extra stable and unstable LCOs, together with low amplitude quasi-periodic oscillations. Such Isola constituted of LCOs greatly restrict the functional range of NES by shrinking the desired domain of attraction.

(IV) Optimization of NES parameters for performance presents consistency in the nonlinear stiffness setup, while a trade-off persists for damping value tuning. However, the NES performance is quite robust to uncertainties/errors in the linear part of damping and stiffness, providing good feasibility for practical applications.

(V) Integration of the SWS into the FVM shows that the NES effectively suppresses shimmy for all four wheels, and simultaneously enhances motion stability of the vehicle body in both dynamical and kinematical senses, which provides a novel solution for passive stability control in advanced chassis design.

Future developments of this work should focus on the elimination of the Isola. For this purpose, the employment of piecewise quadratic damping might be effective, as proposed in [50]. The elimination of the Isola would significantly improve the performance and reliability of the NES for wheel shimmy suppression.

Acknowledgements The authors want to thank Prof. Takacs Denes at the Budapest University of Technology and Economics for his consultations on the nonlinear behavior of wheel shimmy.

Author contributions Hangyu Lu and Giuseppe Habib wrote the main manuscript text and prepared Figs. 1–15. Xiaodong Wu reviewed the manuscript and partially rewrote Sect. 4, and further provided figure 16. Yuankai Ren revised Figs. 1, 4, 6 and corrected the manuscript. Liang Yan provides the test data in Table 1. All authors reviewed the manuscript.

Funding This work was supported by the National 810 Key Research and Development Program of China under Grant 2021YFE0116600. G. Habib acknowledges the financial support of the National Research, Development and Innovation Office (Grant No. NKFI-134496).

Data availibility The data that support the findings of this study are available from the corresponding author, upon reasonable request.

Declarations

Conflict of interest The authors declare that they have no potential conflict of interest.

References

1. Song, P., Tomizuka, M., Zong, C.: A novel integrated chassis controller for full drive-by-wire vehicles. Veh. Syst. Dyn. **53**(2), 215–236 (2015)
2. Murata, S.: Innovation by in-wheel-motor drive unit. Veh. Syst. Dyn. **50**(6), 807–830 (2012)
3. Zhao, Z., Taghavifar, H., Haiping, D., Qin, Y., Dong, M., Liang, G.: In-wheel motor vibration control for distributed-driven electric vehicles: a review. IEEE Trans. Transp. Electr. **7**(4), 2864–2880 (2021)
4. Evangelou, S., Limebeer, D.J.N., Sharp, R.S., Smith, M.C.: Control of motorcycle steering instabilities. IEEE Control Syst. Mag. **26**(5), 78–88 (2006)
5. Besselink, I.J.M.: Shimmy of aircraft main landing gears (2000)
6. Pacejka, H.: Tire and Vehicle Dynamics. Elsevier, New York (2005)
7. Beregi, S., Takács, D., Hős, C.: Nonlinear analysis of a shimmying wheel with contact-force characteristics featuring higher-order discontinuities. Nonlinear Dyn. **90**(2), 877–888 (2017)
8. Takács, D., Stépán, G., John Hogan, S.: Isolated large amplitude periodic motions of towed rigid wheels. Nonlinear Dyn. **52**(1–2), 27–34 (2007)
9. Horvath, H.Z., Takacs, D.: Stability and local bifurcation analyses of two-wheeled trailers considering the nonlinear coupling between lateral and vertical motions. Nonlinear Dyn. **107**(3), 2115–2132 (2021)
10. Hangyu, L., Jianwei, L., Wei, H., Shi, L., Ye, S.: On the nonlinear dynamics of vehicle shimmy coupled with handling motions: modelling, bifurcation analysis, and validations. J. Vib. Control **29**(15–16), 3435–3450 (2022)
11. Ran, S., Besselink, I.J.M., Nijmeijer, H.: Application of nonlinear Tyre models to analyse shimmy. Vehicle Syst. Dyn. **52**(sup1), 387–404 (2014)
12. Ning, Z., Guodong, Y., Nan, C., Tian, M., Pengcheng, L.: A state-of-the-art survey on shimmy problem in vehicle dynamics. J. Mech. Eng. **53**(14), 16–28 (2017)
13. Jianwei, L., Jiang, J., Li, J., Wen, M.: Analysis of dynamic mechanism and global response of vehicle shimmy system with multi-clearance joints. J. Vib. Control **24**(11), 2312–2326 (2018)
14. Zhuravlev, V.Ph., Klimov, D.M., Plotnikov, P.K.: A new model of shimmy. Mech. Solids **48**, 490–499 (2013)
15. Mi, T., Stepan, G., Takacs, D., Chen, N.: Vehicle shimmy modeling with Pacejka's magic formula and the delayed tire model. J. Comput. Nonlinear Dyn. **15**(3), 031005 (2020)
16. Orlando, C., Alaimo, A.: A robust active control system for shimmy damping in the presence of free play and uncertainties. Mech. Syst. Signal Process. **84**, 551–569 (2017)
17. Fallah, M.S., Long, S.H., Xie, W.F., Bhat, R.: Robust model predictive control of shimmy vibration in aircraft landing gears. J. Aircr. **45**(6), 1872–1880 (2008)
18. Tourajizadeh, H., Zare, S.: Robust and optimal control of shimmy vibration in aircraft nose landing gear. Aerosp. Sci. Technol. **50**, 1–14 (2016)
19. Vakakis, A.F., Gendelman, O.: Energy pumping in nonlinear mechanical oscillators: part II-resonance capture. J. Appl. Mech. **68**(1), 42–48 (2001)
20. Gendelman, O.V.: Transition of energy to a nonlinear localized mode in a highly asymmetric system of two oscillators. Nonlinear Dyn. **25**, 237–253 (2001)
21. Ding, H., Chen, L.-Q.: Designs, analysis, and applications of nonlinear energy sinks. Nonlinear Dyn. **100**(4), 3061–3107 (2020)
22. Gendelman, O.V., Sigalov, G., Manevitch, L.I., Mane, M., Vakakis, A.F., Bergman, L.A.: Dynamics of an eccentric rotational nonlinear energy sink. J. Appl. Mech. **79**(1), 011012 (2011)
23. Li, W., Wierschem, N.E., Li, X., Yang, T.: On the energy transfer mechanism of the single-sided vibro-impact nonlinear energy sink. J. Sound Vib. **437**, 166–179 (2018)
24. AL-Shudeifat, M.A., Wierschem, N.E., Bergman, L.A., Vakakis, A.F.: Numerical and experimental investigations of a rotating nonlinear energy sink. Meccanica **52**, 763–779 (2017)
25. Saeed, A.S., AL-Shudeifat, M.A., Vakakis, A.F., Cantwell, W.J.: Rotary-impact nonlinear energy sink for shock mitigation: analytical and numerical investigations. Arch. Appl. Mech. 90:495–521 (2020)
26. Javidialesaadi, A., Wierschem, N.E.: An inerter-enhanced nonlinear energy sink. Mech. Syst. Signal Process. **129**, 449–454 (2019)
27. Wang, J., Wierschem, N., Spencer Jr, B.F., Xilin, L.: Experimental study of track nonlinear energy sinks for dynamic response reduction. Eng. Struct. **94**, 9–15 (2015)
28. Habib, G., Romeo, F.: The tuned bistable nonlinear energy sink. Nonlinear Dyn. **89**(1), 179–196 (2017)
29. Yao, H., Cao, Y., Zhang, S., Wen, B.: A novel energy sink with piecewise linear stiffness. Nonlinear Dyn. **94**, 2265–2275 (2018)
30. Dekemele, K., Habib, G., Loccufier, M.: The periodically extended stiffness nonlinear energy sink. Mech. Syst. Signal Process. **169**, 108706 (2022)
31. Dekemele, K., Habib, G.: Inverted resonance capture cascade: modal interactions of a nonlinear energy sink with softening stiffness. Nonlinear Dyn. 1–23 (2023)
32. Al-Shudeifat, M.A.: Frequency-energy analysis of coupled linear oscillator with unsymmetrical nonlinear energy sink. J. Comput. Nonlinear Dyn. **18**(2), 024501 (2023)
33. Gourdon, E., Lamarque, C.-H., Pernot, S.: Contribution to efficiency of irreversible passive energy pumping with a strong nonlinear attachment. Nonlinear Dyn. **50**, 793–808 (2007)
34. AL-Shudeifat, M.A., Saeed, A.S.: Comparison of a modified vibro-impact nonlinear energy sink with other kinds of NESs. Meccanica **56**, 735–752 (2021)
35. Gendelman, O., Manevitch, L.I., Vakakis, A.F., M'Closkey, R.: Energy pumping in nonlinear mechanical oscillators: part I–dynamics of the underlying Hamiltonian systems. J. Appl. Mech. **68**(1), 34–41 (2001)
36. Gendelman, O.V., Starosvetsky, Yu., Feldman, M.: Attractors of harmonically forced linear oscillator with attached

nonlinear energy sink i: description of response regimes. Nonlinear Dyn. **51**, 31–46 (2008)
37. Lee, Y.S., Vakakis, A.F., Bergman, L.A., Michael McFarland, D., Kerschen, G.: Suppression aeroelastic instability using broadband passive targeted energy transfers, part 1: Theory. AIAA J. **45**(3), 693–711 (2007)
38. Gourc, E., Seguy, S., Michon, G., Berlioz, A., Mann, B.P.: Quenching chatter instability in turning process with a vibro-impact nonlinear energy sink. J. Sound Vib. **355**, 392–406 (2015)
39. Davidson, J., Kalmár-Nagy, T., Habib, G.: Parametric excitation suppression in a floating cylinder via dynamic vibration absorbers: a comparative analysis. Nonlinear Dyn. **110**(2), 1081–1108 (2022)
40. Luongo, A., Zulli, D.: Aeroelastic instability analysis of NES-controlled systems via a mixed multiple scale/harmonic balance method. J. Vib. Control **20**(13), 1985–1998 (2014)
41. Nucera, F., Vakakis, A.F., Michael McFarland, D., Bergman, L.A., Kerschen, G.: Targeted energy transfers in vibro-impact oscillators for seismic mitigation. Nonlinear Dyn. **50**, 651–677 (2007)
42. Habib, G., Kerschen, G.: Suppression of limit cycle oscillations using the nonlinear tuned vibration absorber. Proc. R. Soc. A Math. Phys. Eng. Sci. **471**(2176), 20140976 (2015)
43. Bichiou, Y., Hajj, M.R., Nayfeh, A.H.: Effectiveness of a nonlinear energy sink in the control of an aeroelastic system. Nonlinear Dyn. **86**, 2161–2177 (2016)
44. Habib, G., Epasto, A.: Towed wheel shimmy suppression through a nonlinear tuned vibration absorber. Nonlinear Dyn. **111**(10), 8973–8986 (2023)
45. Sanches, L., Guimarães, T.A.M., Marques, F.D.: Nonlinear energy sink to enhance the landing gear shimmy performance. Acta Mechanica **232**(7), 2605–2622 (2021)
46. Wang, Y., Zhang, T., Jin, X., Yin, Y.: Shimmy suppression of an aircraft nose landing gear using torsional nonlinear energy sink. J. Comput. Nonlinear Dyn. **18**(10), 101002 (2023)
47. Wang, Y., Zhang, T., Yin, Y., Wei, X.: Reducing shimmy oscillation of a dual-wheel nose landing gear based on torsional nonlinear energy sink. Nonlinear Dyn. **112**, 1–36 (2024)
48. Mi, T., Stepan, G., Takacs, D., Chen, N.: Shimmy model for electric vehicle with independent suspensions. Proc. Inst. Mech. Eng. Part D J. Automobile Eng. **232**(3), 330–340 (2018)
49. Daogao, W., Wei, Z., Wenhao, Z., Yinjie, Z., Wei, W., Jiang Ping, W., Bofu, J.H., Jun, L., Andong, Y., et al.: Multiple limit-cycles shimmy characteristics of dual-axle steering mechanism considering the wheel alignment parameters. Proc. Inst. Mech. Eng. C J. Mech. Eng. Sci. **234**(17), 3360–3379 (2020)
50. Starosvetsky, Y., Gendelman, O.V.: Vibration absorption in systems with a nonlinear energy sink: nonlinear damping. J. Sound Vib. **324**(3), 916–939 (2009)